

This is not yet a paper. It is a collection of paper ideas and some preliminary analysis that will make it in to one or more papers.

Data summary: the 7m and 12m data have all been delivered, but the UV coverage is non-optimal. Importantly and unfortunately, no single-dish (total power) data were ever acquired. I have requested APEX observations using the new PI230 instrument to recover the spectral line zero spacings, but that data may not be received for quite some time. The original proposed project connecting cloud scales to core scales will not be possible until the single dish data are acquired.

Subprojects:

1. Core identification and mass estimation and maybe even core mass function constraints. Lead: Ginsburg. This document is a quasi-draft of that work.
2. "A multi-phase outflow from a high-mass protostar" The Lacy jet is detected in both CO and RRLs. This tells us something about its proximity to the HII region IRS2, but what else can we learn from it? Lead: maybe Ginsburg. Maybe this gets incorporated into other papers.
3. Comparative chemistry of the W51 cores. Lead: Victor Rivilla & Maite Beltrán, possibly with participation from Alvaro Sanchez-Monge. This project will involve identifying all of the lines in the W51 cores and examining how the chemistry relates to physical parameters. We will use LTE modeling tools (XCLASS, MAD-CUBA) for many species to identify lines and determine abundances and temperatures
4. H<sub>2</sub>CO and CO turbulent cloud modeling / simulation comparison (Loughnane). A difficulty here is that combination of the 7m and 12m data has not worked out very well yet, either for the lines or the continuum, and that may render cloud-scale analysis quite difficult.
5. A study of the CO outflows. Lead: Maybe Luke Maud? Ciriaco Goddi will be involved. The <sup>12</sup>CO and SO outflows are spectacular and plentiful. It is not obvious whether they can or should be incorporated into this paper; at least, I am not presently prepared to put in the effort to quantify the outflows properly. Ciriaco is PI of a long-baseline program that has resolved the e2/e8 and North cores with 5× better resolution than this program, and that data set may therefore be better suited to a core-outflow association work.
6. Relative kinematics of ionized and molecular gas. Lead: Galván-Madrid. Kinematics similar to ? using RRLs+molecular lines to determine outflow vs infall

## 1. Overview

**This section is not part of any proposed paper text.** The work below will be incorporated into one or more papers as it proves useful. The figures & text represent an initial exploration of the data. There are some important notes that are not included in the text:

- The data reduction has some substantial problems because of strange UV coverage and stranger behavior of clean (for which I have opened many tickets). It appears impossible to get the noise below  $\sim 1$  mJy around the bright sources, and detections are unreliable below  $\sim 10$  mJy in these area (which I've tried to account for when doing source extraction)

- The 7m data does not combine well with the 12m data. It seems to cause major large-angular-scale artifacts. I think this is a weighting issue in which the 7m data have lower noise than the 12m data and are therefore too heavily weighted, causing large "halos" where the large angular scale dominates over the small, providing spuriously strong detections. In principle, this can be solved by downweighting the 7m data, but it turns out CASA does not have that implemented (`innertaper` is the relevant keyword)

## 2. Observations

As part of ALMA Cycle 2 program 2013.1.00308.S, we observed a  $\sim 2' \times 1'$  region centered between W51 IRS2 and W51 e1/e2 with a 37-pointing mosaic. Two configurations of the 12m array were used, achieving a resolution of  $0.2''$ . Additionally, a 12-pointing mosaic was performed using the 7m array, probing scales up to XXX". The full UV coverage was from XX to YY m.

Data reduction was performed using CASA. The QA2-produced data products were combined using the standard inverse variance weighting (check this). The visibilities were imaged into full spectral cubes at coarse ( $0.5''$ ) resolution in order to get a first look at all 15630 spectral channels. The resulting cube was used to identify bright lines in the spectrum extracted from source e8. To produce continuum images, frequency channels including bright lines were excluded.

The spectral setups were ...

### 2.1. Data Reduction

#### 2.1.1. Continuum

A continuum image combining all 4 spectral windows was produced using `tclean`. We phase self-calibrated the image on baselines longer than 100m to increase the dynamic range. The final image was cleaned with 50000 iterations to a threshold of 5 mJy. The lowest noise level in the image, away from bright sources, is  $\sim 0.2$  mJy/beam, but near the bright sources e2 and IRS2, the noise reached as high as  $\sim 2$  mJy/beam. Deeper cleaning was attempted, but lead to instabilities.

#### 2.1.2. Lines

We produced spectral image cubes of the lines listed in Table .... The cubes use only 12m data, as the 12m + 7m combination was unsuccessful.

#### 2.1.3. UV coverage

### 2.2. Morphological Analysis

The largest detected structures include the W51 Main HII region bubble and the W51 IRS2 HII region, which are relatively uninteresting since their properties have been previously well-characterized using radio (JVLA) data. More exciting are the bright dusty structures, especially the "tail" pointing south of W51 e8, which can be described as a 0.25 pc by 0.05 pc filament. This structure has a very high surface brightness along its ridge, exceeding 40 mJy/beam in



**Fig. 1.** A weighted histogram of the visibility weights as a function of UV distance; this approximately shows the amount of data received at each UV spacing

our TE maps ( $23\text{ K}$  or  $3.7 \times 10^4\text{ MJy sr}^{-1}$ ). This high brightness implies a high intrinsic temperature,  $T > 30\text{ K}$  (Section 3.5).

This narrow filament is most prominent in the continuum. It is evident in some lines ( $\text{H}_2\text{CO}$ ,  $^{13}\text{CS}$ ,  $\text{C}^{18}\text{O}$ ), but not others ( $\text{SO}$ , ). It is surrounded by molecular emission that is only slightly fainter... ..in  $\text{SO}$  it's pretty uniform brightness...

### 2.2.1. A bubble around e5

There is evidence of a bubble in the continuum around e5 with a radius of  $6.2''$  ( $0.16\text{ pc}$ ; Figure 2). The bubble is completely absent in the centimeter continuum, so the observed emission is from dust. The bubble edge can be seen from  $58\text{ km s}^{-1}$  to  $63\text{ km s}^{-1}$  in  $\text{C}^{18}\text{O}$  and  $\text{H}_2\text{CO}$ , though it is not continuous in any single velocity channel. There is a collection of compact sources (protostars or cores) along the southeast edge of the bubble.

The presence of such a bubble in dense gas, but its absence in ionizing gas, is surprising. The most likely mechanism for blowing such a bubble is ionizing radiative feedback, especially around a source that is currently a hypercompact HII region, but since no free-free emission is evident within or on the edge of the bubble, it is at least not presently driving the bubble. A plausible explanation for this discrepancy is that e5 was an exposed O-star within the past Myr, but has since begun accreting heavily and there-

fore had its HII region shrunk. This model is marginally supported by the presence of a ‘pillar’ of dense material pointing from e5 toward the south.

The total flux in the north half of the ‘bubble’, which shows no signs of free-free contamination, is about  $1.5\text{ Jy}$ . The implied mass in just this fragment of the bubble is about  $M \sim 350\text{ }M_{\odot}$  for a relatively high assumed temperature  $T = 50\text{ K}$ . The total mass of the bubble is closer to  $M \sim 1000\text{ }M_{\odot}$ , though it may be lower ( $\sim 500\text{ }M_{\odot}$ ) if the southern half is dominated by free-free emission.

With such a large mass, the implied density of the original cloud, assuming it was uniformly distributed over a  $0.2\text{ pc}$  sphere, is  $n(\text{H}_2) \approx 2 - 5 \times 10^5\text{ cm}^{-3}$ .

To evaluate the plausibility of the HII-region origin of the bubble, we compare to classical equations for HII regions. The Strömgren radius is

$$R_s = \left( \frac{3Q_H}{4\pi\alpha_B n^2} \right)^{\frac{1}{3}}. \quad (1)$$

For  $Q_H \sim 10^{49}\text{ s}^{-1}$ ,  $\alpha_B = 3 \times 10^{-13}\text{ cm}^3\text{ s}^{-1}$ ,  $R_s \approx 0.01\text{ pc}$ .

The Spitzer solution for HII region expansion gives

$$R_{\text{HII}}(t) = R_s \left( 1 + \frac{7}{4} \frac{c_{\text{HII}} t}{R_s} \right)^{\frac{4}{7}}. \quad (2)$$

With  $c_{\text{II}} = 7.5 \text{ km s}^{-1}$  and  $t = 10^4 \text{ yr}$ ,  $R_{\text{HII}}(t) \approx 0.04 \text{ pc}$ , while at  $t = 10^5 \text{ yr}$ , it is  $R_{\text{HII}} \approx 0.16 \text{ pc}$ , which is comparable to the observed radius ( $r_{\text{obs}} \sim 0.13 - 0.19 \text{ pc}$ )

Whitworth et al. 1994 give the fragmentation timescale as

$$t_{\text{frag}} \sim 1.56 \left( \frac{c_s}{0.2 \text{ km s}^{-1}} \right)^{\frac{7}{11}} \left( \frac{Q_{\text{H}}}{10^{49} \text{ s}^{-1}} \right)^{-\frac{1}{11}} \left( \frac{n}{10^3 \text{ cm}^{-3}} \right)^{-\frac{5}{11}} \text{ Myr.} \quad (3)$$

Plugging in our numbers gives  $t_{\text{frag}} \approx 1.0 \times 10^5 \text{ yr}$ , or  $10 \times$  longer than the expansion time.

These values are consistent with a late O-type star having been exposed, driving an H II region, for  $\sim 10^4 - 10^5$  year, after which a substantial increase in the accretion rate quenched the ionizing radiation from the star, trapping it into a hypercompact ( $r < 0.005 \text{ pc}$ ) configuration. The recombination timescale is short enough that the ionized gas would disappear almost immediately after the continuous ionizing radiation source was hidden. This is essentially the scenario laid out in ? as an explanation for the compact H II region lifetime problem. In this case, however, it also seems that the H II region has effectively driven the “collect” phase of what will presumably end in a collect-and-collapse style triggering event.

Technically, it is possible that e5 actually represents an optically thick high-mass-loss-rate wind rather than an ultracompact HII region, but I think we can rule this out on physical plausibility considerations if we compare to wind models. Note that  $\eta \text{ Car}$  would have a flux of  $\sim 0.5 \text{ Jy}$  at  $2 \text{ cm}$  and  $\sim 5 \text{ Jy}$  at  $1 \text{ mm}$  at the distance of W51.

### 2.3. Kinematics

We examine the gas kinematics throughout the cloud, but especially near the massive cores.

The ambient cloud, which consists of gas that has not yet condensed into compact prestellar objects, is evident in absorption against the mm cores at  $55\text{--}58 \text{ km s}^{-1}$  (toward e2) and  $57\text{--}60 \text{ km s}^{-1}$  (toward e8). Narrower velocity components related to the known high-velocity streams are detected around  $68 \text{ km s}^{-1}$  toward both sources. These absorption features are seen in all  $\text{H}_2\text{CO}$  transitions,  $\text{CH}_3\text{OH}$   $4_{2,2} - 3_{1,2}$ ,  $\text{OCS}$  18-17, but it was less obvious or absent in  $\text{HNC}$   $10_{1,10} - 9_{1,9}$  and  $\text{OCS}$  19-18.

In the material surrounding the e2 and e8 “cores”, one particularly notable feature is that the cores themselves show a redshifted centroid velocity relative to their surroundings in nearly all of the bright lines ( $\text{H}_2\text{CO}$ ,  $\text{OCS}$ ,  $\text{SO}$ ,  $\text{C}^{18}\text{O}$ ). The observed shift is up to  $\lesssim 2 \text{ km s}^{-1}$ . The shift is a sign of infall. Given the high continuum brightness, the cores are likely optically thick in the continuum (Section ?? XXX), therefore obscuring all molecular emission behind them. We are seeing only gas in the foreground, and this gas is clearly moving toward the cores.

The source ALMamm14 shows a similar kinematic signature....

### 2.4. Simulations

Unfortunately CASA’s simulations produce reproducible incorrectness, in that I cannot get an image

that matches the input image. There seems to \*always\* be some flux scaling no matter what input unit is used. Therefore, I don’t trust any of the results of CASA simulations yet. Perseus looks OK, but Aquila is just flat out wrong, and the scale-recovery simulations I attempted also failed.

**Followup on the above paragraph:** I’ve gotten the simulations worked out; CASA always treats data as if they are in Jy/beam even if Jy/pixel units are specified when using the `sm.predict` module. However, I’m not convinced of their utility at this stage.

The enhanced noise around bright sources is unavoidable. We tested the noise properties of our data set using the CASA `simobserve` toolkit. We obtained a Herschel Gould’s Belt Survey image of the Perseus molecular cloud at  $250 \mu\text{m}$  (resolution  $18''$ ) and scaled it down by  $\sim 40 \times$  to match the resolution of our ALMA data. We used the `sm.predict` task to “observe” the Herschel data with our exact UV data set. We then used `sm.corrupt` to make the noise properties approximately match those of our observations.

We used the Perseus data scaled from  $250 \mu\text{m}$  to  $1.3 \text{ mm}$  assuming a relatively shallow  $\beta = 1.5$  and a constant temperature  $T = 20 \text{ K}$  (since temperature maps are not available). For the Aquila data, we used the column density and temperature maps to derive a synthetic  $1.3 \text{ mm}$  map assuming an opacity  $\kappa_{505\text{GHz}} = 4 \text{ g cm}^{-3}$ . Since Aquila is at a greater distance, the Herschel resolution is coarser ( $0.9''$  at  $5.4 \text{ kpc}$ ) than our best resolution of  $0.2''$ , so it is best compared to lower-resolution tapered data.

When imaging the Perseus data set, we put NGC 1333 at the image center. At the noise levels in our data, only the central portions of NGC 1333 are detected, with three point sources recovered. In this map, the noise properties are very uniform. We are therefore unable to analyze the NGC 1333 data with the exact same parameters as were used on W51. However, using similar parameters (but with a lower significance threshold), we detect only three sources.

In a second experiment, we scaled the peak flux density of the Perseus map to be  $\sim 100 \times$  brighter than it should be, making it comparable to the flux density of W51e2 in the real ALMA observations. In this map, even with deep cleaning, the noise around the bright sources remains very high and artifacts are evident.

## 3. Analysis

### 3.1. Source Identification

We used the `dendrogram` method described by ? and implemented in `astrodendro` to identify sources. We used a minimum value of  $1 \text{ mJy/beam}$  ( $\sim 5 - \sigma$ ) and a minimum  $\Delta = 0.4 \text{ mJy/beam}$  ( $\sim 2 - \sigma$ ) with minimum 10 pixels (each pixel is  $0.05''$ ). This cataloging yielded over 8000 candidate sources, of which the majority are noise or artifacts around the brightest sources. To filter out these bad sources, we created a noise map taking the local RMS of the `tclean`-produced residual map over a  $\sigma = 30$  pixel ( $1.5''$ ) gaussian. We then removed all sources with peak  $\text{S/N} < 8$ , mean  $\text{S/N}$  per pixel  $< 5$ , and minimum  $\text{S/N}$  per pixel  $< 1$ . We also only included the smallest sources in the dendrogram, the “leaves”. These parameters were tuned by checking against “real” sources identified by eye and selected using `ds9`: most real sources are recovered (but not all; see Section ...) and

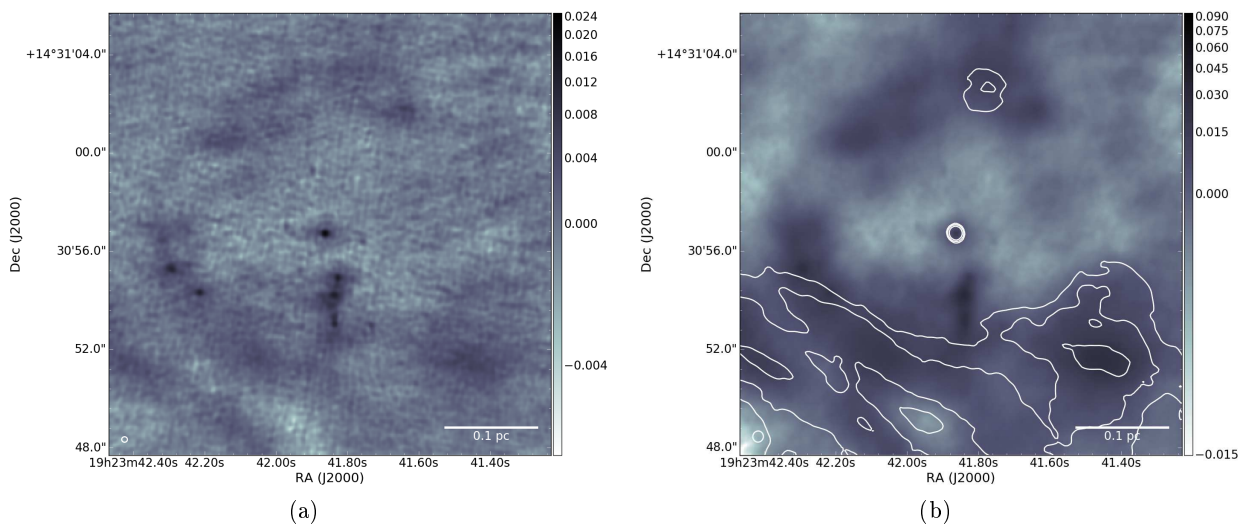


**Fig. 2.** The bubble around source e5. The bubble interior shows no sign of centimeter emission, though the lower-left region of the shell - just south of the “cores” - coincides with part of the W51 Main ionized shell. The source of the ionization is not obvious. (*Left*): A robust -2.0 image with a small ( $0.2''$ ) beam and poor recovery of large angular scale emission. This image highlights the presence of protostellar cores on the left edge of the bubble and along a filament just south of the central source. (*Right*): A robust +2.0 image with a larger ( $0.4''$ ) beam and better recovery of large angular scales. The contours show radio continuum (14.5 GHz) emission at 1.5, 3, and 6 mJy/beam. While some of the detected 1.4 mm emission in the south could be free-free emission, the eastern and northern parts of the shell show no emission down to the  $50 \mu\text{Jy}$  noise level of the Ku-band map, confirming that they consist only of dust emission.

few spurious sources ( $< 10$ ) are included. The resulting catalog includes 113 sources.

The ‘by-eye’ core extraction approach, in which we placed ds9 regions on all sources that look ‘real’, produced a more reliable but less complete (and less quantifiable) catalog. This catalog is more useful in the regions around the bright sources e2 and north, since these regions are affected by substantial uncleaned PSF sidelobe artifacts. In particular, the dendrogram catalog includes a number of sources around e2/e8 that, by eye, appear to be parts of continuous extended emission rather than local peaks; “streaking” artifacts in the reduced data result in their identification despite our threshold criteria.

### 3.2. The spatial distribution of cores

The detected cores are not uniformly distributed across the observed region. The most notable feature in the spatial distribution is their alignment: most of the cores are detected along common lines. This is especially evident in W51 IRS2, where the core density is very high and there is virtually no deviation from the line. The e8 filament is also notably linear, though there are a few sources detected just off the filament.

On a larger scale, the e8 filament points toward e2, apparently tracing a slightly longer filamentary structure. With some imagination, this might be extended along the entire northeast ridge to eventually connect in a broad half-circle with the IRS2 filament (Figure 3). This morphology hints at a possible sequential star formation event, where some central bubble has swept gas into these filaments. However, this ring has no counterparts in ionized gas, and there is little reason to expect such circular symmetry from a real cloud, so the star forming circle may be merely a figment.

Whether it is physical or not, there is a notable lack of cores within the circle. There is no lack of molecular gas, however, as both CO and  $\text{H}_2\text{CO}$  emission fill the full field of view.

### 3.3. Photometry

We created a catalog of the dendrogram sources including their peak and mean flux density, their centroid, and their geometric properties. For each source, we further extracted aperture photometry around the centroid in 6 apertures: 0.2, 0.4, 0.6, 0.8, 1.0, and  $1.5''$ . We performed the same aperture photometry on the W51 Ku-band images from ?. These observations are reported in Table ....

The source flux density distribution is shown in Figure 4. The most common nearest-neighbor separation between cataloged cores is  $\sim 0.3''$ , which implies that the larger apertures double-count some pixels. The smallest separation is  $0.26''$ , so the  $0.2''$  aperture contains only unique pixels.

#### 3.3.1. Distribution Functions

We fit power law distributions to each aperture’s flux distribution. The powerlaws steepen slightly from  $\alpha = 2.0 \pm 0.12$  to  $\alpha = 2.2 \pm 0.16$  for larger apertures. The minimum flux represented by a power law increases from  $\sim 20 \text{ mJy}$  to  $0.4 \text{ Jy}$  ( $14\text{--}280 M_\odot$  at  $20\text{K}$ ). These slopes are shallower than the Salpeter-like slope for the mass function derived by (?) for their sample, though with only modest significance ( $< 3 - \sigma$ ). Of course, these measurements are of the continuum flux density, not directly of the mass, and so a direct comparison may not be appropriate. We revisit this question after assessing the dust temperature in Section 3.5.

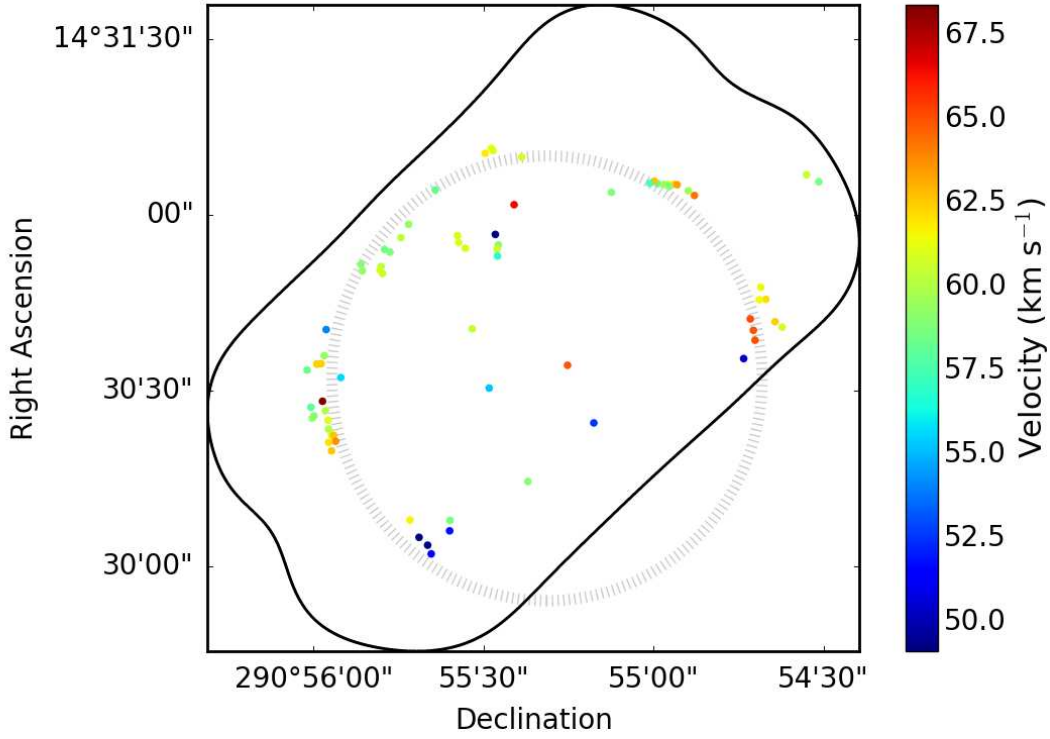


**Fig. 3.** The spatial distribution of the hand-identified core sample. The black outer contour shows the observed field of view. The dashed circle shows a hypothetical ring of star formation.

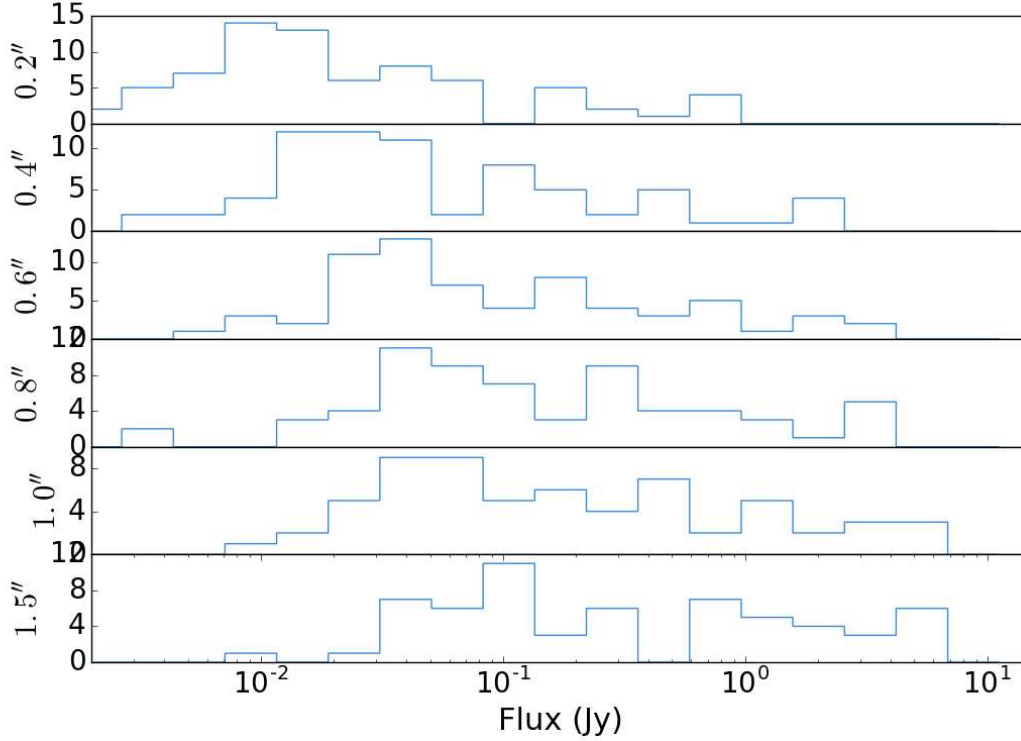


**Fig. 4.** Histograms of the core fluxes measured with circular apertures centered on the hand-extracted core positions. The aperture size is listed in the y-axis label.

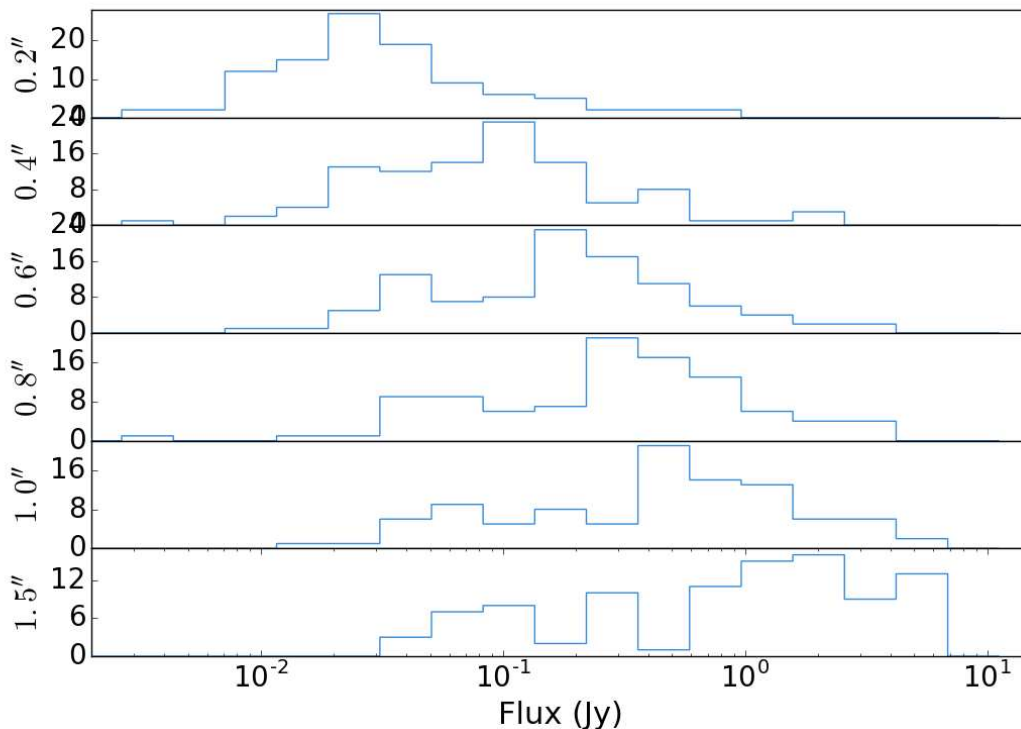


**Fig. 5.** Histograms of the core fluxes measured with circular apertures centered on the dendrogram-extracted core centroids. The aperture size is listed in the y-axis label. Free-free-dominated sources are excluded.

### 3.4. Spectral Lines & Velocities

To determine the line-of-sight velocity of each source, we extracted a spectrum from an  $0.5''$  aperture centered on the source and from a  $0.5$ - $1.0''$  annulus around it. We then searched each spectrum for the brightest pixel and associated it with the likeliest spectral line. We repeated this in each of our 4 spectral windows, then averaged the 4 velocities to get an estimate of the source velocity. This process also allowed us to identify the brightest lines in each window and the brightest overall line observed, which we use later for temperature estimation.

### 3.5. Temperature Estimation

The temperature is a critical ingredient for determining the total mass of each continuum source or region. Since we do not have any means of directly determining the dust temperature, as the SED peak is well into the THz regime and inaccessible with any existing instruments at the requisite resolution, we employ alternative indicators. Above a density  $n \gtrsim 10^5 - 10^6 \text{ cm}^{-3}$ , the gas and dust become strongly collisionally coupled, meaning the gas temperature should accurately reflect the dust temperature. Below this density, the two may be decoupled.

The average dust temperature, as estimated from Herschel Hi-Gal SED fits (??), is 38 K when including the  $70 \mu\text{m}$  data or 26 K when excluding it. This average is obtained over a  $\sim 45''$  ( $\sim 1 \text{ pc}$ ) beam and therefore is likely to be strongly biased toward the hottest dust in the HII regions and around the massive cores, which are known to have temperatures reaching  $> 300 \text{ K}$  (?). Despite these

uncertainties, this bulk measurement provides us with a reasonable range to assume for the uncoupled, low-density dust, which (weakly) dominates the mass (see Section 3.8).

One constraint on the dust temperature we can employ is the absolute surface brightness. For some regions, especially the “filament” and the hot cores noted in Section 2.2, the surface brightness is substantially brighter than is possible for a beam-filling, optically thick blackbody at 20 K, providing a lower limit on the dust temperature ranging from 30 K (40 mJy/beam) to 600 K (1 Jy/beam). Toward most of this emission, optically-thick free-free emission can be strongly ruled out as the driving mechanism using existing data that limits the free-free contribution to be  $< 50\%$  if it is optically thick, and negligible ( $\ll 1\%$ ) if it is optically thin (Ginsburg et al, 2016; Goddi2016a).

To gain a more detailed measurement of the dust temperature in regions where it is likely to be coupled to the gas, we use the peak brightness temperature  $T_{B,max}$  of lines along the line of sight. If the observed molecule is in local thermal equilibrium, as is expected if the density is high enough to be coupled to the dust for many molecules, and it is optically thick, the brightness temperature provides an approximate measurement of the true physical temperature near the  $\tau = 1$  surface. If any of these assumptions do not hold,  $T_{B,max}$  will set a lower limit on the true gas temperature. Only nonthermal maser emission would push  $T_{B,max} > T_{gas}$ .

One potential problem with this approach is if the gas becomes optically thick before probing most of the dust. Some transitions, e.g. CO and  $\text{H}_2\text{CO}$ , are likely to be affected by this issue.

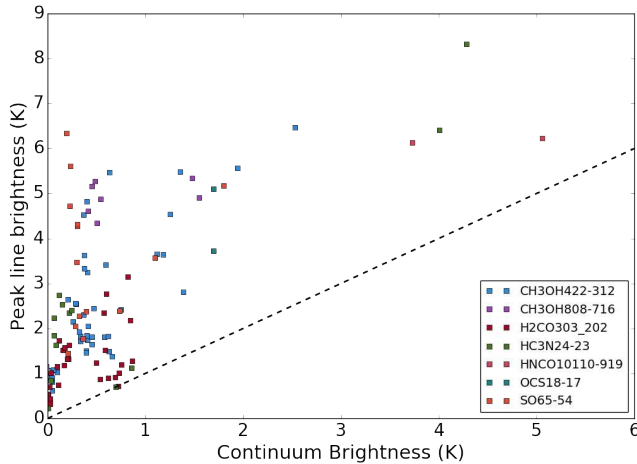


**Fig. 6.** The peak line brightness vs the continuum brightness of our target sources within  $\sim 1''$  beams. The points are color-coded by the brightest observed line. The dashed line shows where the brightness temperature of the continuum matches that of the lines; technically this means that it should be impossible for any point to be below the line.

### 3.6. The most massive protostellar cores in W51

In Figure 7, we show the radial profiles extracted from the three high-mass protostellar cores in W51: W51 North, W51 e2e, and W51 e8. The plot shows the enclosed mass out to  $\sim 1''$  (5400 AU). On larger spatial scales, the enclosed mass rises more shallowly, indicating the end of the core (though our data are capable of recovering spatial scales up to XXXXX).

All three sources show similar radial profiles, containing up to  $3000 M_{\odot}$  within a very compact radius of 5400 AU (0.03 pc). However, the temperature structure within these sources is certainly not homogeneous, and very likely a large fraction of the total flux comes from  $T \gtrsim 300$  K heated material (Section 3.5 ?). If the observed dust were all at 600 K, the mass would be  $\sim 17\times$  lower,  $100 M_{\odot}$ , which we treat as a strict lower bound as it is unlikely that the dust more than  $\gtrsim 1000$  au is so warm. Additionally, it is very likely that a substantial mass of cold dust is also present but undetectable because it is hidden by the hotter dust.

### 3.7. The most massive prestellar cores in W51

To place limits on the most massive prestellar cores, we need to know the temperature of the dust in all of the bright ( $> 15$  mJy;  $10 M_{\odot}$  at 20 K) sources. We do not have any direct means of evaluating the dust temperature, but we can infer at least a lower limit on it by determining the peak brightness temperature of an optically thick line that is excited at densities  $n \gtrsim 10^5 \text{ cm}^{-3}$ , at which the dust and gas are coupled.

To accomplish this, we have found the brightest lines across the full  $\sim 6\text{GHz}$  spectra and measured their peak brightness temperature.

**TODO:** use coarser resolution ( $2'' = 0.1 \text{ pc}$ ?) data to extract “cores” where no smaller (protostellar) cores are detected. Try to estimate their masses. These are the best candidate “prestellar” cores, though likely anything this large is likely to be a massive cluster...

### 3.8. The mass budget on different spatial scales

An important evolutionary indicator is the amount of mass at a given density; a more evolved (more efficiently star-forming) region will have more mass at high densities. We cannot measure the dense gas fraction directly, but the amount of flux density recovered by an interferometer provides a reasonable approximation.

For the “total” flux density in the region, we use the Bolocam Galactic Plane Survey observations (??), which are the closest in frequency single-dish millimeter data available. We assume a spectral index  $\alpha = 3.5$  to convert the BGPS flux density measurements at 271.4 GHz to the mean ALMA frequency of 226.6 GHz. The ALMA data (specifically, the 0.2'' 12m-only data) have a total flux 23.2 Jy above a very conservative threshold of 10 mJy/beam in our mosaic; in the same area the BGPS data have a flux of 144 Jy, which scales down to 76.5 Jy. The recovery fraction is  $30 \pm 3\%$ , where the error bar accounts for a change in  $\alpha \pm 0.5$ . The threshold of 10 mJy/beam corresponds to a column threshold  $N > 10^{25} \text{ cm}^{-3}$  for 20 K dust. For an unresolved spherical source, this corresponds to a volume density  $n > 10^{8.1} \text{ cm}^{-3}$ .

**TODO:** determine the largest angular scale in the ALMA images. Requires using the simulations.

### 3.9. Chemically Distinct Regions

The “hot cores” in W51 are resolved and multi-layered.

Surrounding W51e2e, we noted the presence of sharp-edged uniform-brightness regions in a few spectral lines over the range  $51\text{--}60 \text{ km s}^{-1}$  (Figure 8). These features are elongated in the direction of the outflow, but have significant extend orthogonal to the outflow, spanning  $9500 \times 6600$  AU. They are prominent in  $\text{CH}_3\text{OH}$ ,  $\text{OCS}$ , and  $\text{CH}_3\text{OCH}_3$ , weak but present in  $\text{H}_2\text{CO}$  and  $\text{SO}$ , and absent in  $\text{HC}_3\text{N}$  and  $\text{HNC}$ .

Around e8, a similar feature is observed, but this time  $\text{CH}_3\text{OCH}_3$  is absent.

Along the south end of the e8 filament, no such enhanced features are seen; only  $\text{H}_2\text{CO}$  and the lowest transition of  $\text{CH}_3\text{OH}$  are evident.

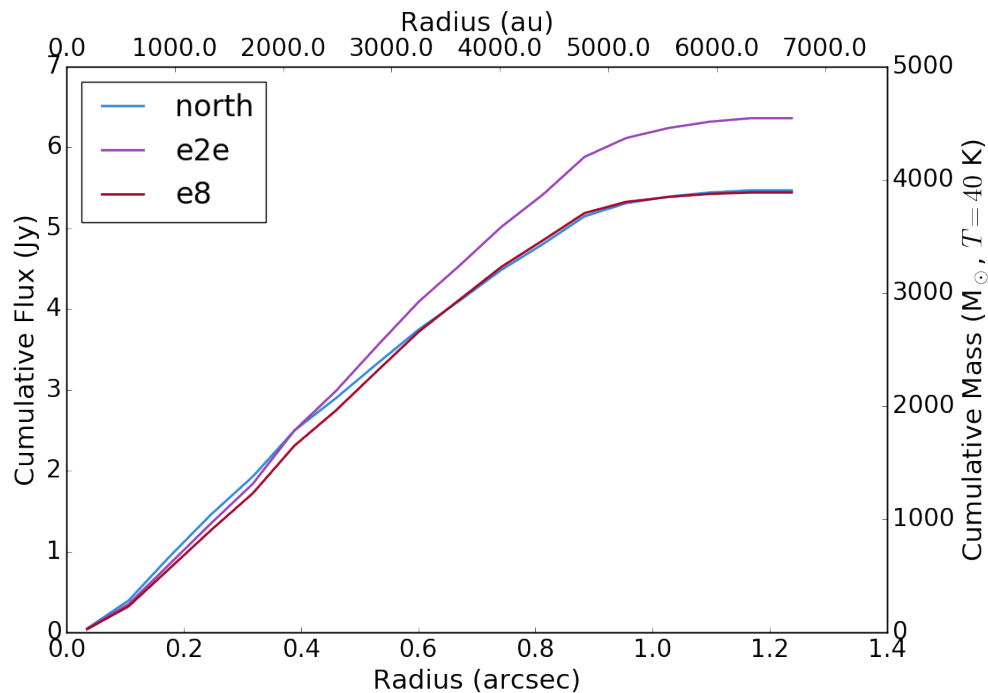


**Fig. 7.** The cumulative flux density radial profiles centered on three massive protostellar cores. They share similar profiles and are likely dominated by hot dust in their innermost regions, but they are more likely to be dominated by cooler dust in their outer, more massive regions.

Toward W51 north,  $\text{CH}_3\text{OH}$ ,  $\text{H}_2\text{CO}$ , and  $\text{SO}$  exhibit the sharp-edged enhancement feature, while the other species do not. The enhancement is from  $50\text{--}60\text{ km s}^{-1}$ .

Given the enhanced abundance of  $\text{CH}_3\text{OH}$  in particular, it seems likely that these sharp-edged bubbles represent sublimation zones in which substantial quantities of grain-processed materials are released into the gas phase. The sharp edges likely reflect the particular point where the temperature exceeds the sublimation temperature for each species.

The relative chemical structures of e2, e8, and IRS2 are relatively similar. The same species are detected in all of the central cores. However, in e2,  $\text{CH}_3\text{OCH}_3$ ,  $\text{CH}_3\text{OCHO}$ ,  $\text{CH}_3\text{CH}_2\text{CN}$ , and Acetone ( $[\text{CH}_3]_2\text{CO}$ ) are significantly more extended in e2 than in the other sources.  $g\text{-CH}_3\text{CH}_2\text{OH}$  is detected in W51 North, but is weak in e8 and almost absent in e2.

The substructure of different species in e2 is also revealing. Species that are elongated in the NW/SE direction are associated primarily with the outflow ( $\text{HC}_3\text{N}$ ,  $\text{CH}_3\text{CH}_2\text{CN}$ ). Other species are associated primarily with the extended core ( $\text{CH}_3\text{OCHO}$ ,  $\text{CH}_3\text{OCH}_3$ ,  $[\text{CH}_3]_2\text{CO}$ ). Some are only seen in the compact core ( $\text{H}_2\text{CN}$ ,  $\text{HNCO}$ ,  $\text{NH}_2\text{CHO}$ , and vibrationally excited  $\text{HC}_3\text{N}$ ). Only  $\text{CH}_3\text{OH}$  and  $\text{OCS}$  are associated with both the extended core and the outflow, but not the greater extended emission.  $\text{H}_2\text{CCO}$  seems to be associated with only the extended core, but not the compact core. Finally, there are the species that trace the broader ISM in addition to the cores and outflows ( $\text{H}_2\text{CO}$ ,  $^{13}\text{CS}$ ,  $\text{OCS}$ ,  $\text{C}^{18}\text{O}$  and  $\text{SO}$ ). Both  $\text{HCOOH}$  and  $\text{N}_2\text{D}^+$  are weak and associated only with the innermost e2e core.





**Fig. 8.** Moment 0 maps of the e2 region in 40 different lines over the range 51 to 60  $\text{km s}^{-1}$  with continuum subtraction using the 30th percentile emission over the ranges 25-40 and 75-90  $\text{km s}^{-1}$ . All images are on the same scale, and the negative features show absorption against the continuum. There is a strong ‘halo’ of emission seen in the  $\text{CH}_3\text{Ox}$  lines and OCS. Extended emission is also clearly seen in SO,  $^{13}\text{CS}$ , and  $\text{H}_2\text{CO}$ , though these lines more smoothly blend into their surroundings. HNCO and  $\text{NH}_2\text{CHO}$  have smaller but substantial regions of enhancement with a sharp contrast to their surroundings.  $\text{HC}_3\text{N}$  traces the e2 outflow. The bright  $\text{H}30\alpha$  emission marks the position of e2w, the hypercompact HII region that dominates the centimeter emission in e2.



**Fig. 9.** Moment 0 maps of the e8 region in 40 different lines over the range 52 to 63  $\text{km s}^{-1}$  with continuum subtraction using the 30th percentile emission over the ranges 25-40 and 75-90  $\text{km s}^{-1}$ . All images are on the same scale, and the negative features show absorption against the continuum. As in e2, there is extended emission in the  $\text{CH}_3\text{OH}$  and OCS lines, but in contrast, the other  $\text{CH}_3\text{Ox}$  lines are more compact. SO is brighter than OCS in e8, whereas the opposite is true in e2.

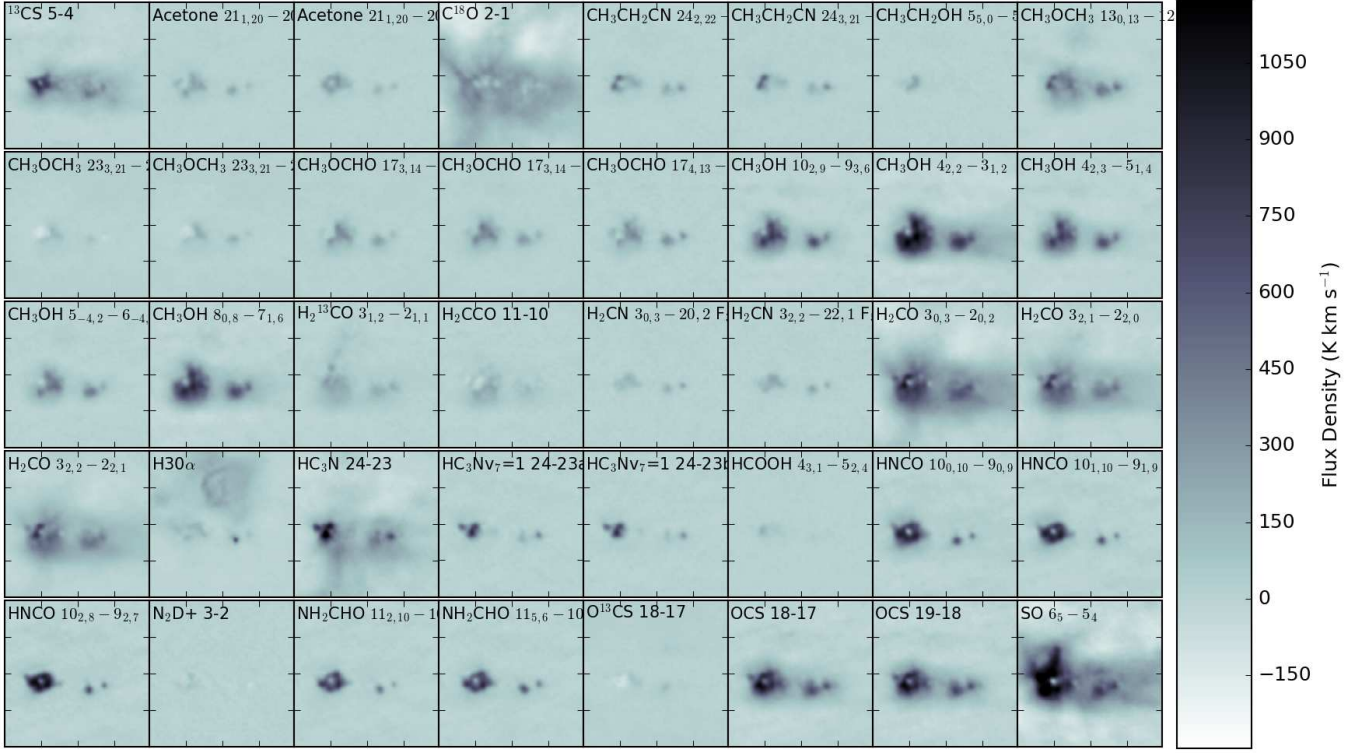


**Fig. 10.** Moment 0 maps of the W51 IRS2 region in 40 different lines over the range 54 to 64 km s<sup>-1</sup> with continuum subtraction using the 30th percentile emission over the ranges 25-40 and 75-90 km s<sup>-1</sup>. All images are on the same scale, and the negative features show absorption against the continuum. Qualitatively, the relative extents of species seem comparable to e8. The H30α point source is W51 d2.



**Fig. 11.** Moment 0 maps of the ALMamm14 region in 40 different lines over the range 58 to 67 km s<sup>-1</sup> with continuum subtraction using the 30th percentile emission over the ranges 25-40 and 75-90 km s<sup>-1</sup>. All images are on the same scale. ALMamm14 is one of the brightest sources outside of e2/e8/IRS2, but it is substantially fainter than those regions. Still, it has a noticeably rich chemistry.

#### 4. Outflows

We detected many outflows in CO and SO.



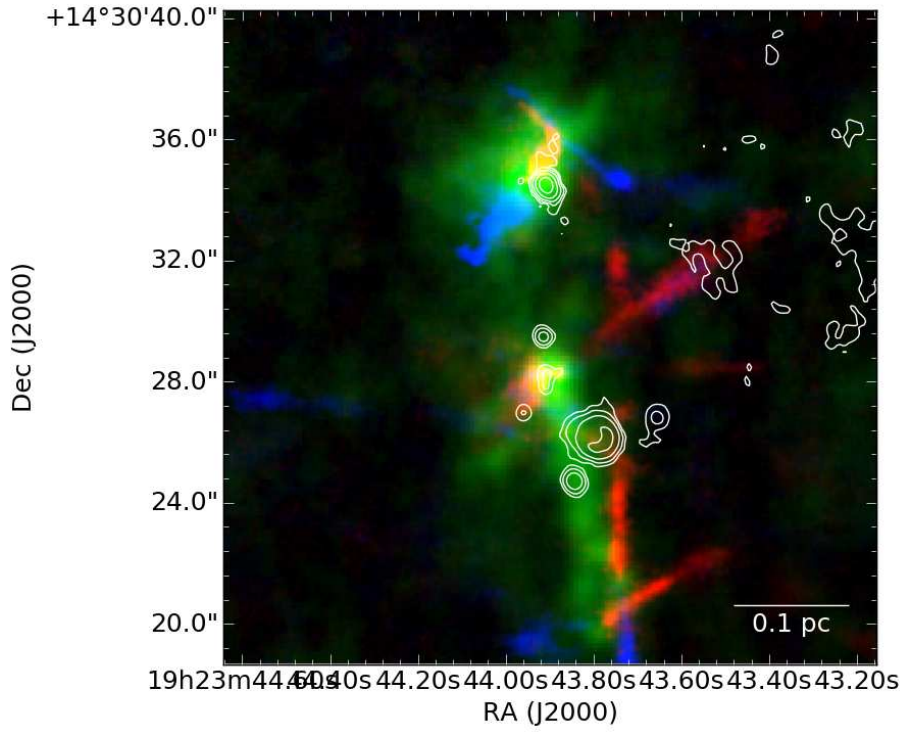


**Fig. 12.** Outflows in red and blue overlaid on mm continuum in green with cm continuum contours in white.



**Fig. 13.** Outflows in the W51 IRS2 region. The green emission is NACO K-band continuum, with ALMA 1.4 mm continuum contours in white and H77 $\alpha$  contours in blue. The ? jet is prominent in H77 $\alpha$ .